



This is a repository copy of *Six-Phase Fractional-Slot-per-Pole-per-Phase Permanent-Magnet Machines With Low Space Harmonics for Electric Vehicle Application*.

White Rose Research Online URL for this paper:
<http://eprints.whiterose.ac.uk/110284/>

Version: Accepted Version

Article:

Patel, V.I., Wang, J. orcid.org/0000-0003-4870-3744, Wang, W. et al. (1 more author) (2014) Six-Phase Fractional-Slot-per-Pole-per-Phase Permanent-Magnet Machines With Low Space Harmonics for Electric Vehicle Application. *IEEE Transactions on Industry Applications*, 50 (4). pp. 2554-2563. ISSN 0093-9994

<https://doi.org/10.1109/TIA.2014.2301871>

© 2014 IEEE. Personal use of this material is permitted. Permission from IEEE must be obtained for all other users, including reprinting/ republishing this material for advertising or promotional purposes, creating new collective works for resale or redistribution to servers or lists, or reuse of any copyrighted components of this work in other works. Reproduced in accordance with the publisher's self-archiving policy.

Reuse

Unless indicated otherwise, fulltext items are protected by copyright with all rights reserved. The copyright exception in section 29 of the Copyright, Designs and Patents Act 1988 allows the making of a single copy solely for the purpose of non-commercial research or private study within the limits of fair dealing. The publisher or other rights-holder may allow further reproduction and re-use of this version - refer to the White Rose Research Online record for this item. Where records identify the publisher as the copyright holder, users can verify any specific terms of use on the publisher's website.

Takedown

If you consider content in White Rose Research Online to be in breach of UK law, please notify us by emailing eprints@whiterose.ac.uk including the URL of the record and the reason for the withdrawal request.



eprints@whiterose.ac.uk
<https://eprints.whiterose.ac.uk/>

6-phase Fractional Slot per Pole per Phase Permanent Magnet Machines with Low Space Harmonics for Electric Vehicle Application

Vipulkumar I. Patel, Student Member, IEEE, Jiabin Wang, Senior Member, IEEE, Weiya Wang, and Xiao Chen, Student Member, IEEE

Abstract—The paper discusses the development of new winding configurations for 6-phase permanent magnet (PM) machines with 18-slot, 8-pole, that eliminates and/or reduces undesirable space harmonics in the stator magneto motive force (MMF). The proposed configuration improves power/torque density and efficiency with a reduction in eddy current losses in the rotor permanent magnets and copper losses in end windings. To improve drive train availability for applications in electric vehicles, the paper proposes the design of 6-phase permanent magnet machine as two independent 3-phase windings. A number of possible phase shifts between two sets of 3-phase windings due to their slot-pole combination and winding configuration is investigated and the optimum phase shift is selected by analyzing the harmonic distributions and their effect on machine performance including the rotor eddy current losses. The machine design is optimized for a given set of specifications for electric vehicle (EV), under electrical, thermal and volumetric constraints, and demonstrated by the experimental measurements on a prototype machine.

Index Terms— Design methodology, Design optimization Electric vehicles, Permanent magnet machines.

I. INTRODUCTION

RECENTLY, the development of fault tolerant motor drives employing permanent magnet (PM) machines for electric vehicles (EV) has received increasing attention due to the emphasis on passenger comfort and safety by the automotive industries around the world [1]-[4]. Although electric vehicles are hailed as fuel economic and low- or no-emissions, their ability to tolerate fault is very critical as a fault in the electric drive will result in a complete loss of power and may lead to an accident [2]. Due to their high torque/power density and higher efficiency compared to other machine technologies, PM brushless machines are preferred technology in traction applications [5],[6], provided they could continue to operate following isolated failures in power train drive.

For traction applications, it is an attractive option to employ

Manuscript received August 10, 2013; revised October 12, 2013. This work was supported in part by the European Commission for CASTOR project under European Green Cars Initiative through Grant No. 260176.

V. I. Patel, J. Wang, W. Wang, and X. Chen are with the Department of Electronic and Electrical Engineering, The University of Sheffield, Sheffield, S1 3JD, United Kingdom (e-mail: vip.iitd@outlook.com, j.b.wang@sheffield.ac.uk).

relatively newer winding configurations of PM brushless machines often referred to as fractional-slot concentrated winding or modular winding [6]-[9], because of their numerous advantages over the overlapped distributed windings in the conventional brushless AC machines, such as high winding factor, high copper packing factor [10], short end-windings, and hence, high efficiency [11], reduction in the likelihood of an inter-phase fault and extremely low cogging torque [12].

However, fractional-slot windings produce a large number of space harmonics in the stator magneto-motive-force (MMF) [6],[7]. The lower and higher order space harmonics in the stator MMF rotate at different speeds relative to the rotor, and hence cause many undesirable effects that include localized core saturation, eddy current losses in the permanent magnets, acoustic noise and vibrations [13],[14]. These space harmonics also make it difficult to obtain high reluctance torque from interior permanent magnet (IPM) machines with fractional-slot windings [15].

Among a number of techniques reported in the literature to mitigate the above detrimental effects, the most common approach is to segment the rotor magnets both axially and circumferentially in order to reduce the eddy current loss on the rotor [16]. Without this, the heat generated by the eddy current loss in the rotor magnets may be excessive and may result in irreversible demagnetization [17]. However, this significantly increases the manufacturing cost and material usage (materials being wasted during segmentation process), and does not address the other undesirable effects.

G. Dajaku et al. [18] have reported a new 24-slot, 10-pole machine topology to reduce the sub- and high stator MMF harmonics of the conventional 12-slot, 10-pole fractional slot windings by dividing the 3-phase windings into two sets and placing an appropriate phase shift between the two. However, this is achieved with a small reduction of the winding factor for the fundamental EMF component, which compromises the torque density and efficiency, while the first space harmonic is not much affected. To reduce these harmonics, further methods have been described in [19] by (a) using different number of turns per coil for the neighboring phase coils or (b) employing coil windings with different number of turns per coil side. This leads to uneven stator tooth width and more complex winding configuration with further reduction in the

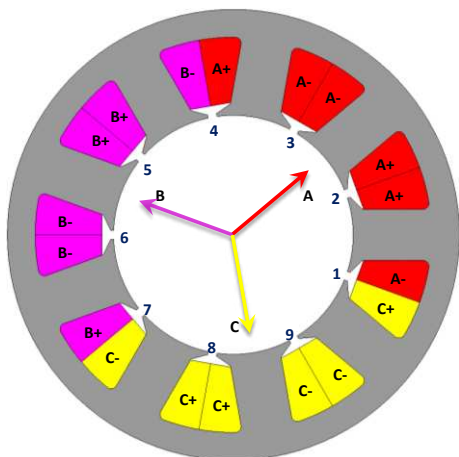


Fig. 1. Schematic of 3-phase, 9-slot, 8-pole winding configuration

fundamental EMF winding factor. An alternate approach to reduce the most harmful MMF space harmonics (1^{st} and 7^{th}) is described in [20] by developing 18-slot, 10-pole winding configuration with two sets of concentric windings with star-delta connections, which helps in reducing radial force mode of the machine by completely eliminating 7^{th} MMF space harmonics. However, this configuration has very low winding factor for fundamental EMF (~ 0.76) and employs different number of turns for star and delta windings, which impose challenges to achieve (a) higher torque density, and (b) ease of manufacturing.

The concept of stator shifting is investigated in [21] to assess its effect on various harmonic components of stator MMF, winding factor, power density and efficiency (both at low speeds and in flux-weakening region) as well as torque ripple for various slot-pole combinations of fractional slot PM machines. This technique works more effectively in designs with a single sub-harmonic, whereas the improvement is compromised for slot-pole combinations having multiple sub-harmonics. Also, it introduces uneven tooth width in the stator, which may lead to reduction of peak torque capability due to uneven flux density levels in stator teeth.

In order to eliminate the most harmful space harmonics in a simple and cost-effective way, a novel fractional-slot per pole, per phase winding configuration for 3-phase electrical machines has been devised by Wang et al. [22]. This winding configuration is applicable to a range of electrical machine technologies, viz., permanent magnet machines, induction machines, synchronous wound-field machines and synchronous reluctance machines; and also improves both torque/power density and efficiency of these different machine technologies for a variety of applications. A full comparison of this machine topology with conventional fractional-slot machines has been reported in [23] for permanent magnet assisted synchronous reluctance machines.

To improve safety and availability in traction applications, multiple 3-phase motor drives are advantageous [24]. Compared to conventional 3-phase motor drives, the multiple 3-phase motor drives are inherently fault tolerant [25], as loss of one 3-phase system will not lead to a complete loss of

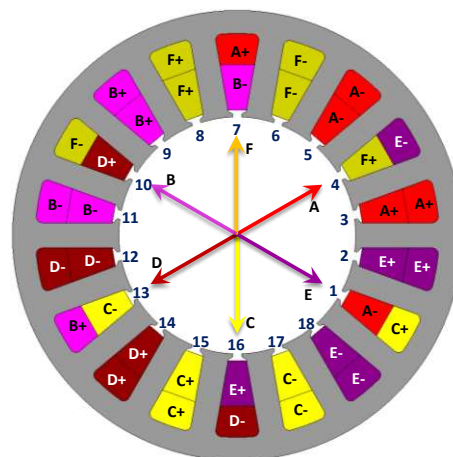


Fig. 2. Schematic of 6-phase, 18-slot, 8-pole winding configuration

traction power. In addition, they have lower torque ripples, lower current per phase for the same voltage, lower dc link current harmonics and improved torque per ampere capability [2].

The aim of this paper is to develop a 6-phase machine configured as two independently controlled 3-phase systems using the proposed 3-phase fractional-slot per pole, per phase winding configuration with low space harmonics [22], and to investigate the optimum phase shift between two sets of 3-phase windings in the 6-phase permanent magnet machine. This winding arrangement is specifically designed to enhance availability of the traction drive.

II. 6-PHASE FRACTIONAL SLOT PER POLE PER PHASE WINDING CONFIGURATION WITH LOW SPACE HARMONICS

A. Development of 6-phase, 18-slot, 8-pole Winding

Many feasible slot - pole combinations exist for fractional-slot per pole per phase machines [26], [27]. The 9-slot, 8-pole winding configuration inherently suffers from presence of large space harmonics in the stator MMF and unbalanced magnetic forces [14]. In order to reduce the undesirable space harmonics significantly and to eliminate unbalanced magnetic forces associated with 9-slot, 8-pole combination, and any other combination derived from its integer multiple, this paper uses the proposed technique for 3-phase machine in [22] to develop 6-phase, 18-slot, 8-pole winding configuration.

Fig. 1 shows the schematic of 3-phase, 9-slot, 8-pole winding configuration found in the prior art, whereas the schematic of the proposed winding configuration with 6-phase, 18-slot, 8-pole is shown in Fig. 2.

Each phase winding consists of three series connected coils wired around two adjacent teeth with the polarity as indicated by "+" and "-". The stator windings which are inserted in the stator slots comprise 6 phases denoted as A, B, C, D, E, and F in Fig. 2. The coil span is two slot-pitches and the mechanical angle between two coil-sides is $360^\circ/9 = 40^\circ$.

The second 3-phase windings (D-E-F) are positioned with respect to the first 3-phase windings (A-B-C) by an offset of 180° mechanical or 9 slot-pitches. The offset in electric

degrees is 720° or 4π . Thus if phase windings A and D are arranged with the same polarity, and similar arrangements are made for B and E, and C and F, respectively, the resultant 4th order MMF space harmonics produced by the first 3-phase windings (A-B-C) and the second 3-phase windings (D-E-F) are in phase with respect to each other. The 4th order space harmonic interacts with the 4 pole-pair rotor magnetic field to produce the electromagnetic torque. For all odd ($n = 1, 3, 5, \dots$) space harmonics, the phase shift between the harmonics produced by the first 3-phase winding and those by the second 3-phase winding is $n \cdot \pi$. Thus these harmonics have the same magnitude but in the opposite direction and hence will be cancelled with each other by the proposed winding scheme.

Thus, the winding configuration shown in Fig. 2 results in the highest possible winding factor of 0.945 for the 4th order working space harmonic, and completely eliminates all odd space harmonics. The end-windings are slightly longer than conventional tooth windings, whereas it is much shorter than distributed windings. Also, the end-windings of different phase coils, being in parallel, can be easily insulated using coil separators, which in turn reduce the likelihood of interphase faults. Further, the normal magnetic force produced by the first 3-phase windings is cancelled by that produced by the second 3-phase windings, thereby; eliminating unbalanced magnetic pull in the radial direction, which are conducive for reducing bearing loss, noise and vibration.

B. MMF Profile of 6-phase, 18-slot, 8-pole Winding Configuration

Fig. 3 shows the MMF profile of A-B-C and D-E-F windings of 6-phase, 18-slot, 8-pole machine when the currents in D-E-F are displaced from those in A-B-C by 180° electrical. Fig. 4 shows the combined MMF profile of 6-phase, 18-slot, 8-pole winding configuration. The resultant MMF space harmonics distribution is shown in Fig. 5 along with that of 3-phase, 9-slot, 8-pole winding configuration. As will be seen, all odd space harmonics have cancelled in the 6-phase, 18-slot, 8-pole winding configuration. The remaining undesirable harmonics have relatively low magnitude except for the 2nd, 14th and 22nd harmonics. As the frequency of the 2nd harmonics seen by the rotor is relatively low, the resultant undesirable effect is also significantly less. The 14th and 22nd harmonics will be attenuated rapidly in the radial direction towards the rotor because of their shorter wavelengths. Hence, the undesirable effects caused by these harmonics will be much less significant.

C. Optimal Phase Shift between Two Sets of 6-Phase, 18-slot, 8-pole Winding Configuration

Conventionally, 6-phase machines employing distributed windings have phase shift of 60° between each phase. This configuration can also be seen as two sets of 3-phase windings with a phase shift of 180° between the sets.

With the proposed winding configuration, it is possible to have different phase shifts between two sets of 3-phase windings than the conventional phase shift of 180° . Table I summarizes all 18 possible phase shifts between two sets of 3-

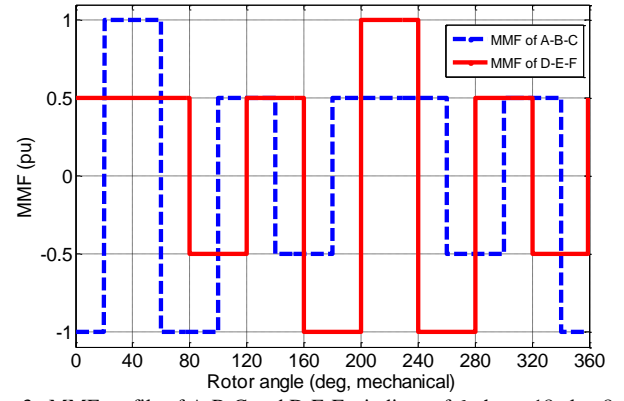


Fig. 3. MMF profile of A-B-C and D-E-F windings of 6-phase, 18-slot, 8-pole machine

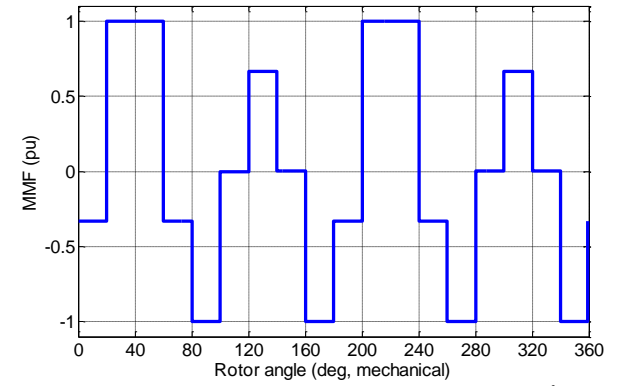


Fig. 4. MMF profile of 6-phase, 18-slot, 8-pole machine with 180° electrical phase shift between A-B-C and D-E-F windings

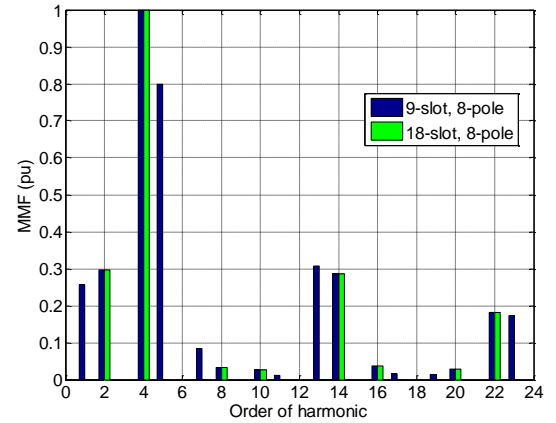


Fig. 5. Comparison of normalized MMF space harmonics distribution

TABLE I
POSSIBLE PHASE SHIFTS IN 6-PHASE, 18-SLOT, 8-POLE WINDING CONFIGURATION

| D-E-F polarity same as A-B-C | | D-E-F polarity opposite to A-B-C | |
|------------------------------|-------------|----------------------------------|-------------|
| Slot-shift | Phase shift | Slot-shift | Phase shift |
| α_s | θ | α_s | θ |
| 1 | 80° | 1 | 260° |
| 3 | 240° | 3 | 60° |
| 5 | 40° | 5 | 220° |
| 7 | 200° | 7 | 20° |
| 9 | 0° | 9 | 180° |
| 11 | 160° | 11 | 340° |
| 13 | 320° | 13 | 140° |
| 15 | 120° | 15 | 300° |
| 17 | 280° | 17 | 100° |

TABLE II
REDUCED PHASE SHIFTS IN 6-PHASE, 18-SLOT, 8-POLE WINDING CONFIGURATION

| Slot-shift | Phase shift between A-B-C and D-E-F |
|------------|-------------------------------------|
| α_s | θ |
| 3-9-15 | 0° |
| 1-7-13 | 20° |
| 5-11-17 | 40° |

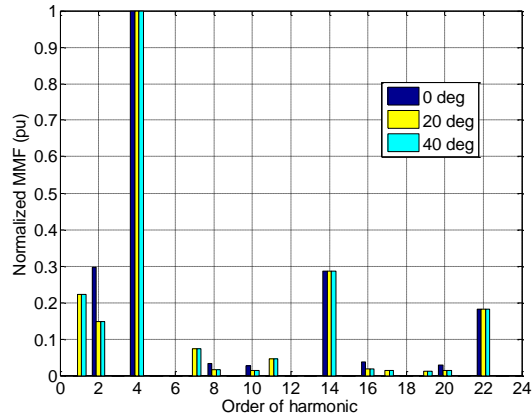


Fig. 6. Comparison of normalized MMF space harmonics distribution for various phase shifts between A-B-C and D-E-F in 6-phase, 18-slot, 8-pole winding configuration

TABLE III
TOTAL HARMONIC DISTORTION FOR VARIOUS PHASE SHIFTS

| Phase shift | T.H.D. (all n) | T.H.D. (n = 1-100) | T.H.D. (n = 1-30) |
|-------------|----------------|--------------------|-------------------|
| θ | | | |
| 0° | 51.8% | 50.5% | 45.6% |
| 20° | 50.2% | 48.8% | 43.8% |
| 40° | 50.8% | 49.4% | 44.4% |

phase windings. By analyzing the vector diagrams of all phases with all possible phase shifts [21], it can be shown that the 18 possible phase shifts are reduced to only 3 different phase shifts as listed in Table II.

The phase shifts listed in Table II result into balanced windings irrespective of whether the machine is operated with 6-phases or just one set of 3-phase. This feature enhances the capability of the winding configuration for traction application as it is inherently fault tolerant. In the event of a fault on one set of 3-phase, other set of 3-phase will continue to operate as a balanced machine with half the torque/power output.

Fig. 6 shows the normalized MMF space harmonics distribution for the three different phase shifts between A-B-C and D-E-F. As seen, the proposed winding configuration with 0° phase shift eliminates all odd space harmonics that are present in the 9-slot 8-pole winding configuration, therefore results in much improved performance. The effect of 20° and 40° phase shifts is the same – both help in reducing the 2nd harmonics by ~50%, however, gives rise to other odd harmonics (1st, 7th, and 11th) that were otherwise not present with 0° phase shift. However, these odd harmonics are less significant due to their lower frequency (for 1st) or lower magnitude (for 7th and 11th).

Table III lists the total harmonic distortion (THD) of all three phase shifts between A-B-C and D-E-F. It is evident that

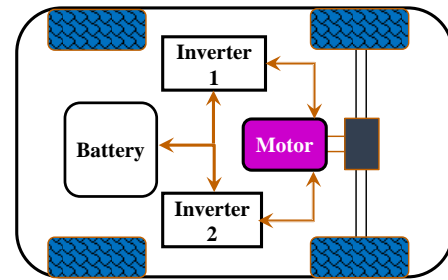


Fig. 7. Configuration of power drive train for electric vehicle

TABLE IV
DESIGN SPECIFICATIONS OF THE TRACTION MOTOR

| Specification | Symbol | Value |
|---|---------------|-----------|
| No. of phases | q | 6 |
| Base speed | ω_b | 2800 rpm |
| Maximum cruise speed | ω_{ms} | 11000 rpm |
| Maximum speed | ω_m | 12000 rpm |
| Peak torque below and at base speed | T_{pk} | 140 N·m |
| Rated torque below and at base speed | T_c | 75 N·m |
| Peak power at base speed | P_{pk-b} | 41 kW |
| Peak power at maximum cruise speed | P_{pk-ms} | 32 kW |
| Continuous rated power | P_c | 22 kW |
| Peak torque at maximum cruise speed | T_{ms} | 27.8 N·m |
| Continuous torque at maximum cruise speed | T_{mc} | 19.1 N·m |
| Nominal DC link voltage | V_{dc} | 320 V |
| Maximum line-line voltage | E_m | 650 V |
| Cooling medium | - | Water |

the THD ($n = 1$ to 30) of 20° phase shift is 1.8% and 0.6% lower than that of 0° and 40° phase shift respectively. Lower THD of 20° phase shift will result into comparatively lower rotor iron loss including PM eddy current loss. Hence, 20° phase shift is selected as optimum phase shift for the 6-phase machine, and it is realized by 13 slot-shifts between A-B-C and D-E-F. This winding configuration is employed to design permanent magnet synchronous motor for EV application.

III. MOTOR DESIGN SPECIFICATIONS & CONSTRAINTS

A. Drive Train and Motor Design Specifications

The traction machine for a segment-A vehicle with centralized drive is considered using the proposed winding configuration with 6-phase, 18-slot, 8-pole. The vehicle employs one traction motor coupled to the front or rear axle via a differential and a reduction gearbox as shown in Fig. 7. The 6-phases of the electric traction motor are controlled as two separate and independent 3-phase systems, which are fed by two separate inverters. In the event of a fault on one of the drive system, the vehicle can continue to operate using the remaining set of 3-phase drive system without any sudden stops or compromising vehicle stability and passenger safety.

From the vehicle data and acceleration performance requirements, the design specifications for the motor can be obtained [28], which are listed in Table IV.

Among numerous PM machine topologies that are derived from the arrangement of PM in the rotor structure, a surface mounted permanent magnet (SPM) motor and interior permanent magnet motor (IPM) are most commonly used [29]. The magnets in SPM machines are directly exposed to stator

TABLE V
DESIGN CONSTRAINTS FOR THE TRACTION MOTOR

| Design Parameter | Symbol | Constraints |
|------------------------------|-----------|------------------------------------|
| Stator outer radius | RAD2 | 75 mm |
| Stack length of the motor | L_{stk} | ≤ 150 mm |
| Continuous current density | J_c | ≤ 10 A/mm ² |
| Maximum flux linkage | ψ_m | ≤ 74.7 mWb |
| Maximum motor current - peak | I_m | ≤ 200 A |
| d-axis inductance | L_d | $0.256 \leq L_d \leq 0.721$ mH |
| Copper winding temperature | T_{cu} | $\leq 180^\circ\text{C}$ (class H) |
| Steel lamination temperature | T_{fe} | $\leq 225^\circ\text{C}$ |
| Permanent magnet temperature | T_{pm} | $\leq 150^\circ\text{C}$ (NdFeB) |

MMF space harmonics, and segmentation of magnets in circumferential and axial direction may be necessary to reduce the eddy current loss. Also, a metallic sleeve or glass/carbon fiber banding layer is required in order to contain magnets in SPM machines. Both of these lead to increased manufacturing cost. On the other hand, in IPM machines, as PM are buried inside the rotor slots and shielded by the rotor core, segmentation may not be necessary. IPM machines also have better field-weakening capability which is often desirable for EV traction. However, detailed mechanical and structural analysis is required to ensure the structural integrity of the rotor, which increases the design cycle time. In this paper, an IPM machine with the proposed winding configuration is employed for the EV application.

B. Design Constraints for EV Traction Motor

In addition to the design specifications, thermal, electrical and volumetric constraints are given in Table V. The flux linkage due to permanent magnets (ψ_m) must be constrained to limit the voltage below the maximum permissible peak line-line voltage in the event of an inverter fault, $V_{m-line-line} < E_m$. The maximum peak motor current (I_m) is limited by the inverter VA rating. The torque ripple must be below 5% for passenger comfort and ease of noise and vibration harness (NVH). In addition, the d-axis inductance must be kept with a maximum and minimum range [30] in order to satisfy the constant power profile given in Table IV.

IV. DESIGN OPTIMIZATION OF 6-PHASE, 18-SLOT, 8-POLE, IPM MOTOR

For a given stator radius of 75 mm and stack length of 150 mm, the geometrical parameters that have most significant influence on the performance are shown in Fig. 8, which include rotor radius RAD1, magnet pole arc β_m , magnet cap depth IPMHQ, length of magnet LM, width of magnet per pole MAGWID, slot depth SD, and stator tooth width TWS. The slot opening SO and stator slot opening depth TGD are considered to fine tune the d-axis inductance. It should be noted that the required stator tooth width TWS, and yoke depth, which is a function of SD and RAD1, are dependent on the air-gap flux density and maximum permissible flux density in the teeth and yoke.

Generally, the performance of a PM machine enhances as LM is increased. This, however, increases the cost of the machine. Therefore, the mass of PM is to be minimized against the design specifications and demagnetization

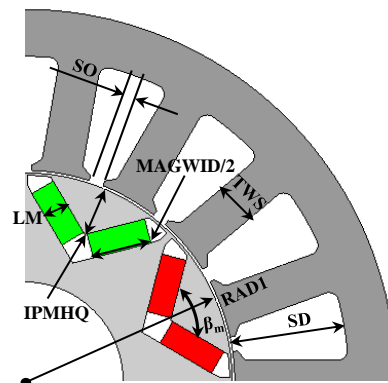


Fig. 8. Cross-section of 6-phase, 18-slot, 8-pole IPM with influential geometrical parameters

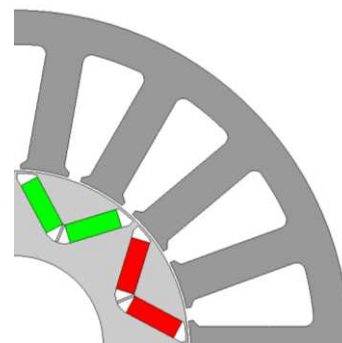


Fig. 9. Cross-section of optimized 6-phase, 18-slot, 8-pole IPM motor

withstand-ability under the worst case condition. The air gap length is assumed to be constant, at 0.5 mm considering the manufacturing tolerances, and static and dynamic radial clearances. M270-35A electrical steel is used for the stator and the rotor laminations, whereas the permanent magnet material NdFeB is considered with remanent flux density and relative recoil permeability of 1.1T and 1.04 respectively.

A. Design Optimization

It is important to note that since the EV operates over a wide torque speed range, a design optimized against the rated torque at the base speed does not necessarily lead to an optimal design over a given driving cycle [31]. Likewise, a design optimized against a driving cycle does not yield the best performance when a different drive cycle or condition takes place. Thus, similar to the design of conventional ICE vehicles, the design and performance are very much dependent on drive styles. Hence, the objective of the optimization was to achieve the best possible torque production at the base speed whilst minimizing the losses over the representative driving cycle, i.e. New European Driving Cycle (NEDC).

The leading design parameters are optimized against the objectives subject to the specifications and constraints through a combination of analytical and 2-D finite element analysis (FEA).

Because of high speed operation requirements for this traction motor, the mechanical stress analysis is carried out using 2-D FEA at 1.5 times the maximum speed (i.e. 18000 rpm) as part of the design optimization to arrive at the best possible post and bridge geometry of the IPM motor, which

TABLE VI
GEOMETRICAL PARAMETERS OF THE MOTOR

| Parameter | Symbol | Unit | Initial Design | Opt. Design |
|---------------------------|---------------|-----------------|----------------|-------------|
| Rotor radius | RAD1 | mm | 39.25 | 39.00 |
| Stator slot depth | SD | mm | 28.50 | 27.82 |
| Stator tooth width | TWS | mm | 8.30 | 8.38 |
| Stator slot opening | SO | mm | 3.0 | 3.0 |
| Stator slot opening depth | TGD | mm | 1.0 | 1.0 |
| Stator slot area | | mm ² | 283.6 | 269.2 |
| Length of PM | LM | mm | 5.0 | 4.2 |
| Width of PM per pole | MAGWID | mm | 24.0 | 24.0 |
| Turns per coil | t_c | | 12 | 10 |
| No. of coils per phase | N_{cp} | | 3 | 3 |
| Mass of PM material | M_{PM} | kg | 1.066 | 0.900 |
| NEDC Energy efficiency | η_{NEDC} | % | 94.4 | 94.9 |

TABLE VII
STEADY STATE TEMPERATURE OF MOTOR COMPONENTS

| Component | Design Limit | Temperature |
|---------------------------|--------------|-------------|
| Copper windings - average | 180°C | 97.7°C |
| Permanent magnet | 150°C | 142.7°C |
| Stator steel – at bore | 225°C | 94.6°C |
| Rotor steel – maximum | 225°C | 143.1°C |

not only keeps the rotor stresses well below the yield strength of rotor material but also provides support to PM during operation. The iterative process between mechanical design and electromagnetic design was carried out to arrive at best design that is within mechanical stress design limit with best electromagnetic performance. Fig. 9 shows the cross-section of the optimized motor. Table VI compares the geometrical parameters obtained after initial design with those of the final design optimization using 2-D FEA.

It is vital to consider thermal behavior of the motor during the design iterations to ensure the various components of the motor do not exceed thermal design limits. The thermal analysis can be carried out at various load points. However, the motor design must satisfy the thermal design limits (listed in Table VII) at maximum cruise speed with continuous operation. This operating condition, 19.1 N•m at 11000 rpm, referred to the maximum cruise speed operation, represents the maximum continuous power consumption of the vehicle.

Table VII shows the steady-state temperature of various motor components at the maximum cruise operation. It is evident that the steady state temperature of all motor components is within the design limit. The rotor temperature is much higher than that of the stator due to the fact that at high speeds, the eddy current loss in the rotor core is relatively large as a result of high operating frequency. The majority of the rotor loss has to be dissipated to the stator via the air gap which exhibits large thermal resistance and, hence, lead to high temperature difference between the rotor and the stator.

B. Performance of the Optimized Motor

The performance of the optimized motor is evaluated for the rated and the peak torque operation at the base speed and is shown in Table VIII. The energy efficiency over the NEDC is calculated using energy center of gravity principle [32].

Fig. 10 shows the torque ripple over an electrical cycle of the optimized motor at the rated and the peak torque operation,

TABLE VIII
PERFORMANCE OF THE OPTIMIZED MOTOR

| | Unit | Rated Torque | Peak Torque |
|---------------------------------|-------------------|--------------|-------------|
| Torque | N•m | 75.0 | 140.0 |
| Torque ripple | % | 2.5 | 4.2 |
| Speed | rpm | 2800 | 2800 |
| Peak current | A | 74.0 | 172.5 |
| Voltage (V_{line-1}) | V | 217.0 | 298.0 |
| Current density | A/mm ² | 9.7 | 22.7 |
| Copper loss / Iron loss | W | 809 / 181 | 4394 / 273 |
| PM eddy current loss | W | 8 | 56 |
| Efficiency | % | 95.7 | 89.7 |
| Energy efficiency over the NEDC | % | 94.9 | |

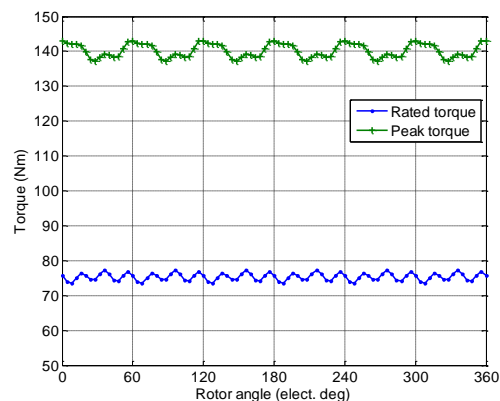


Fig. 10. Torque waveform of optimized motor at base speed of 2800 rpm

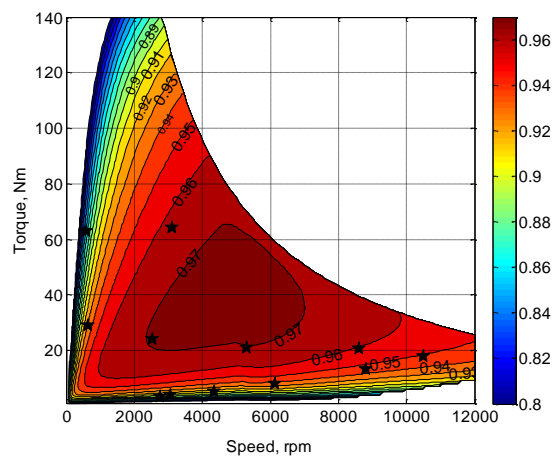


Fig. 11. Predicted efficiency map of optimized 6-phase, 18-slot, 8-pole IPM motor

which is below the requirement of 5% for EV applications.

The predicted efficiency map of the motor derived from FEA is shown in Fig. 11. The representative 12 points of NEDC for motor specifications listed in Table IV are also shown as stars. It is evident that the designed IPM motor has high efficiency over wide torque-speed range of the traction vehicle.

V. PROTOTYPE AND EXPERIMENTAL VALIDATION

A prototype machine employing the novel 6-phase, 18-slot, 8-pole winding configuration has been constructed to validate the design for the given specifications of electric vehicle mentioned in Table IV. Fig. 12 (a) shows the stator and the

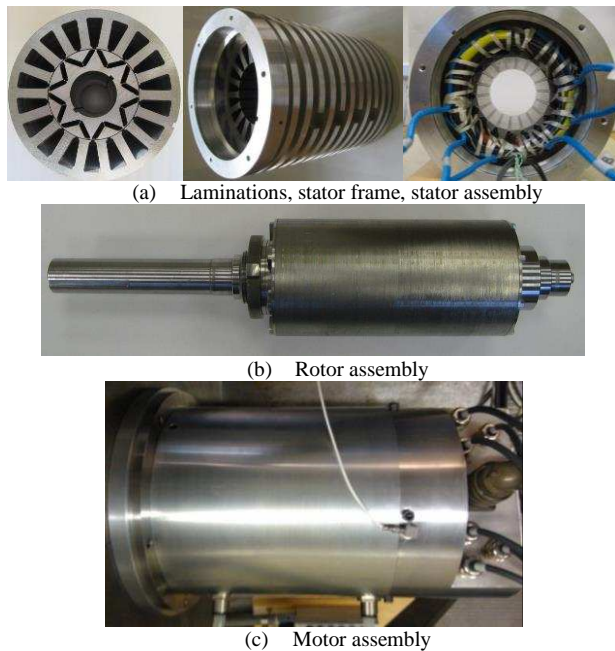


Fig. 12. Components of the prototype machine employing 6-phase, 18-slot, 8-pole winding configuration having 20° electrical phase shift between A-B-C and D-E-F

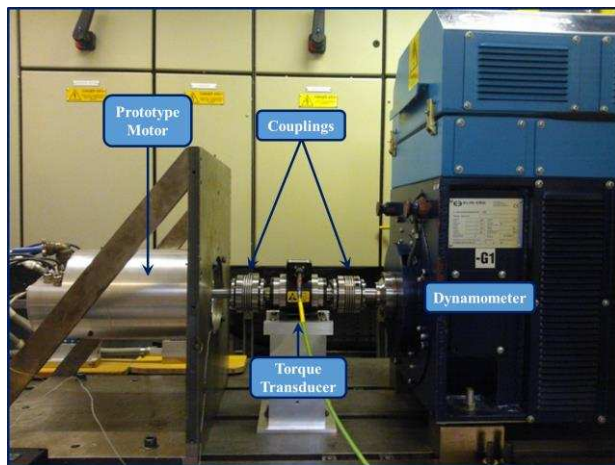


Fig. 13. Prototype motor coupled to the dynamometer on test rig with in-line torque transducer

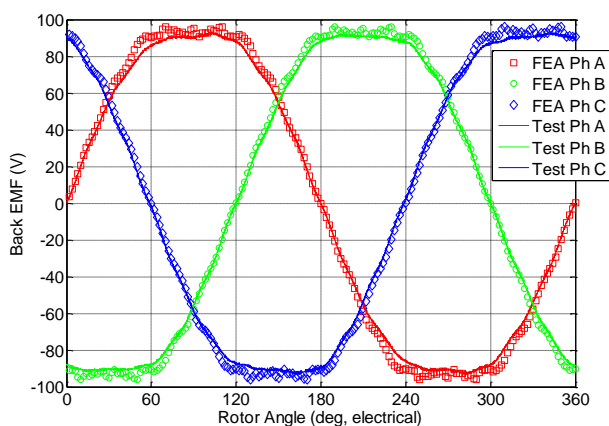


Fig. 14. Comparison of measured and predicted back-EMF of A-B-C windings of 6-phase, 18-slot, 8-pole IPM machine at base speed of 2800 rpm

rotor laminations, stator frame with cooling chamber, and stator assembly; whereas rotor assembly and motor assembly of the prototype motor are shown in Fig. 12 (b) and (c) respectively. The prototype motor is equipped with thermocouples and thermistors to measure temperature of various components, and light weight, voltage mode accelerometer to monitor vibrations during the tests.

The performance of the prototype machine has been measured on the test rig shown in Fig. 13. As seen, the prototype motor is coupled to the dynamometer using backlash-free, torsion-ally stiff metal below couplings and an in-line torque transducer. The dynamometer, which is controlled by a bidirectional four-quadrant converter, is used to drive the motor at a given speed and provides load torque during the load test. The motor is controlled by a 6-phase inverter configured as two independent 3-phase inverters that operates in torque control mode and can achieve flux-weakening operation in a high-speed range. The inverter dc-link power is fed by a programmable bi-directional dc power supply. The 6-phase input power to the motor (from the inverter) is measured by a power analyzer via the high-precision ($\pm 0.02\%$ accuracy for power reading), high-bandwidth voltage and zero-flux current transducers. The motor output power is obtained through the in-line torque transducer (accuracy of $< \pm 0.1\%$, temperature sensitivity of ± 0.2 N·m/10K, range 0 – 200 N·m) by measuring the torque and speed. The test rig shown in Fig. 13 allows direct and precise measurements of the motor efficiency.

Fig. 14 compares the measured and the FE predicted back-EMF waveforms of the A-B-C windings of the 6-phase machine at the base speed of 2800 rpm. Similar measured and predicted waveforms are obtained for D-E-F windings but are not plotted for clarity of the illustration. The FE prediction was made with the permanent magnet property based on the data sheet of the magnet supplier for the room temperature at which the back EMF was measured. From the comparison, it is found that the RMS and peak values of the measured back-EMF are 2.7% and 2.4% lower than the prediction respectively. This can be attributed to lower permanent magnet length (LM) in the prototype due to grinding or tolerance requirements for inserting them inside the rotor, as shown in Fig. 9, and the resulting air-gap between the magnets and rotor core, as well as slightly different BH characteristics of the magnets and the laminations between the datasheet and the actual materials used in the prototype.

The no-load loss tests with the prototype rotor and a dummy rotor were carried out using the in-line torque transducer with an accuracy of $\pm 0.1\%$ and temperature sensitivity of ± 0.02 N·m/10K for the range of 0.1 N·m – 20 N·m. The dummy rotor has the same mass and mechanical dimensions as the prototype rotor. The no-load iron loss is therefore obtained by subtracting the no-load loss with the dummy rotor from that with the prototype rotor. Fig. 15 shows the comparison of predicted and measured no-load iron loss from standstill to maximum cruise speed. It can be seen that by introducing a build factor of 1.32 that accounts for any deterioration of material properties of laminations, the calibrated no-load iron

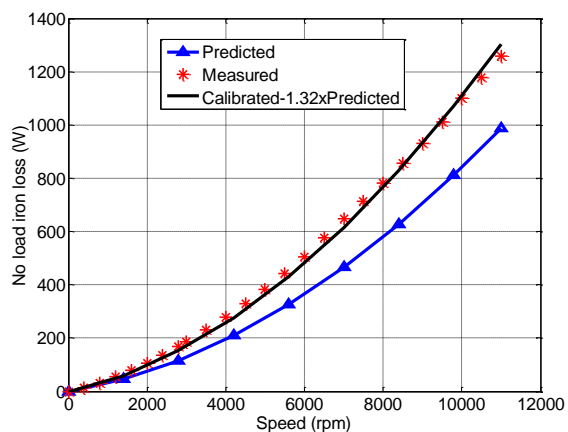


Fig. 15. Comparison of measured and predicted no-load iron loss

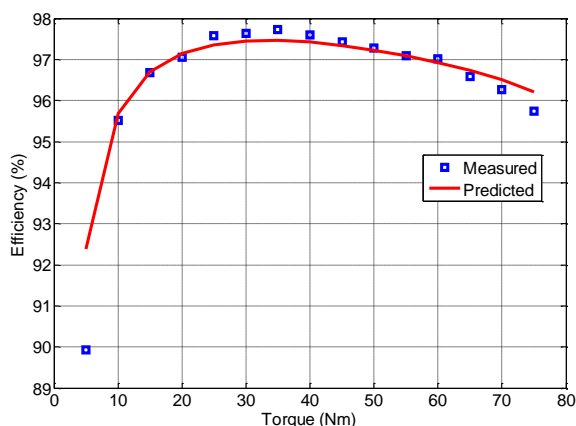


Fig. 16. Comparison of measured and predicted efficiency of prototype IPM machine at base speed of 2800 rpm

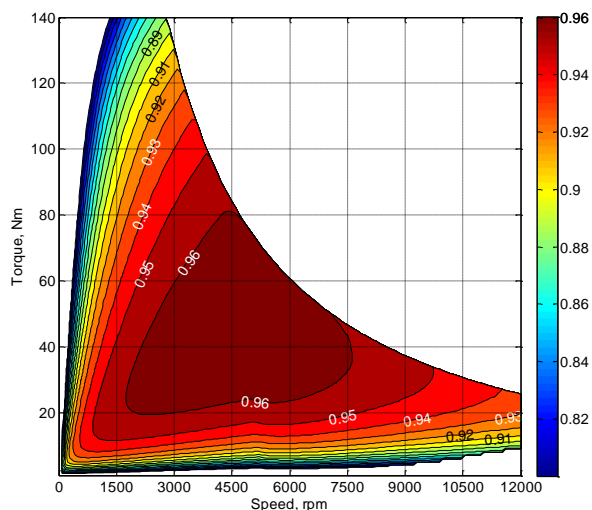


Fig. 17. Calibrated efficiency map of the prototype IPM machine based on test measurements

loss model matches very well with the measured no-load iron loss.

The load tests were carried out to evaluate the motor and drive operation and to measure their efficiency within the torque-speed envelope. Fig. 16 compares the measured and the

predicted efficiency at the base speed of 2800 rpm. As observed, at the load torque of 5 N·m, the measured efficiency is ~2.5% lower than the prediction. This is mainly due to lower accuracy of torque transducer at low torque level, and the friction and windage losses which are not accounted in the prediction. At load torque greater than 60 Nm, the measured efficiency is again slightly lower than the prediction. This is likely due to slightly lower measured back-EMF as shown in Fig. 14 and under-estimation of iron loss prediction for the machine. The difference between the measured and the predicted efficiency at medium torque levels is very small and can be attributed to the combined effect of torque transducer accuracy, the error in copper and iron loss predictions, and mechanical losses due to friction and windage, which are neglected in the prediction.

Based on the measured efficiency map over discrete points, the computational model for predicting losses over the torque-speed envelope is calibrated by considering (a) the measured resistance of the windings (3% increase), (b) a build factor of 1.32 for iron loss derived from no-load iron loss test data and (c) the measured friction and windage loss. Fig. 17 shows the calibrated efficiency map of the prototype motor. Compared to the predicted efficiency map in Fig. 11, the efficiency is reduced by up to 1% mainly due to the three factors. Also, at higher speeds as the quality of current control in the field-weakening region deteriorates slightly due to voltage saturation, the reduction in efficiency is more than that at lower speeds.

VI. CONCLUSION

This paper has presented a novel 6-phase fractional slot per pole per phase IPM motor with a slot-pole combination (18-slot, 8-pole) which exhibits high winding factor and eliminates all odd-order space harmonics which are otherwise present in conventional fractional slot windings. The availability of traction drive is enhanced by designing 6-phase motor as two independent 3-phase windings. The optimized design of the IPM motor with the new winding configuration exhibits high efficiency over a wide speed range and enhanced availability for EV applications. The experimental results with the prototype machine have validated the proposed new winding configuration. It should be emphasized that this winding configuration is applicable for a range of electrical machine technologies for a variety of applications.

ACKNOWLEDGMENT

The authors thank John A. Wilkinson for his valuable support during the research work at The University of Sheffield, UK, and gratefully acknowledge the European Commission and CASTOR project partners for permission of the publication of this paper.

REFERENCES

- [1] N. Bianchi, M. D. Pre, and S. Bolognani, "Design of a fault-tolerant IPM motor for electric power steering," *IEEE Trans. on Vehicular Technology*, Vol. 55, No. 4, pp. 1102-1111, Jul. 2006.

- [2] M. T. Abolhassani, and H. A. Toliyat, "Fault tolerant permanent magnet motor drives for electric vehicles," IEEE International Electric Machines & Drives Conference (IEMDC), pp. 1146-1152, May 2009.
- [3] Q. Chen, G. Liu, W. Gong, and W. Zhao, "A New Fault-Tolerant Permanent-Magnet Machine for Electric Vehicle Applications," IEEE Trans. on Magnetics, Vol.47, No.10, pp.4183-4186, Oct. 2011.
- [4] G. Liu, W. Gong, Q. Chen, L. Jian, Y. Shen, and W. Zhao, "Design and analysis of new fault-tolerant permanent magnet motors for four-wheel-driving electric vehicles," Journal of Applied Physics, Vol.111, No.7, pp.07E713-07E713-3, Apr. 2012.
- [5] Z. Q. Zhu, and D. Howe, "Electrical machines and drives for electric, hybrid and fuel cell vehicles," Proc. of the IEEE, Vol. 95, No. 4, pp. 746-765, Apr. 2007.
- [6] J. Wang, K. Atallah, Z. Q. Zhu, and D. Howe, "Modular 3-phase permanent magnet brushless machines for in-wheel applications," IEEE Trans. on Vehicular Technology, Vol. 57, No. 5, pp. 2714-2720, Sep. 2008.
- [7] J. Wang, X. P. Xia, and D. Howe, "Three-phase modular permanent magnet brushless machine for torque boosting on a down-sized ICE vehicle," IEEE Trans. on Vehicular Technology, Vol. 54, No. 3, pp. 809-816, May 2005.
- [8] K. Atallah, J. Wang, and D. Howe, "Torque ripple minimisation in modular permanent magnet brushless machines," IEEE Trans. on Industry Applications, Vol. 36, No.6, pp. 1689-1695, Nov.-Dec. 2003.
- [9] J. Cros, and P. Viarouge, "Synthesis of high performance PM motors with concentric windings," IEEE Trans. on Energy Conversion, Vol. 17, No. 2, pp. 248-253, Jun. 2002.
- [10] T. Oikawa, T. Tajima, K. Matsumoto, H. Akita, H. Kawaguchi, and H. Kometani, "Development of high efficiency brushless DC motor with new manufacturing method of stator for compressors", Sixteenth International Compressor Engineering Conference, Purdue, USA, CD12-4, 2002.
- [11] A. G. Jack, B.C. Mecrow, P.G. Dickinson, and D. Stephenson, "Permanent-magnet machines with powdered iron cores and prepressed windings", IEEE Trans. on Industry Applications, Vol. 36, No.4, pp. 1077-1084, Jul.-Aug. 2000.
- [12] Z. Q. Zhu, and D. Howe, "Influence of design parameters on cogging torque in permanent magnet machines," IEEE Trans. on Energy Conversion, vol. 15, no. 4, pp. 407-412, Dec. 2000.
- [13] N. Bianchi, S. Bolognani, M. D. Pre, and G. Grezzani, "Design considerations for fractional-slot winding configurations of synchronous machines," IEEE Trans. on Industry Applications, Vol. 42, No. 4, pp. 997-1006, Jul.-Aug. 2006.
- [14] Z.Q. Zhu, D. Ishak, D. Howe, and J. Chen, "Unbalanced magnetic forces in permanent magnet machines with diametrically asymmetric disposition of phase windings," IEEE Trans. on Industry Applications, Vol. 43, No. 6, pp. 1544-1553, Nov.-Dec. 2007.
- [15] J. K. Tangudu, T. M. Jahns, and A. El-Refai, "Unsaturated and Saturated Saliency Trends in Fractional-Slot Concentrated-Winding Interior Permanent Magnet Machines," Proc. of IEEE Energy Conversion Congress and Exposition (ECCE), pp. 1082-1089, Sep. 2010.
- [16] J. D. Ede, K. Atallah, G. Jewell, J. Wang, and D. Howe, "Effect of axial segmentation of permanent magnets on rotor loss in modular permanent magnet brushless machines," IEEE Trans. on Industry Applications, Vol. 43, No. 5, pp. 1207-1213, Sep.-Oct. 2007.
- [17] J. Wang, W. Wang, K. Atallah, and D. Howe, "Demagnetization Assessment for 3-phase Tubular Brushless Permanent Magnet Machines," IEEE Trans. on Magnetics, Vol. 44, No. 9, pp. 2195-2203, Sep. 2008.
- [18] G. Dajaku, "Elektrische Maschine" German patent, DE 102008 057 349 B3, July 15, 2010.
- [19] G. Dajaku, and D. Gerling, "A novel 24-slots/10-poles winding topology for electric machines," Proc. of IEEE International Electric Machines and Drives Conference (IEMDC), pp. 65-70, May 2011.
- [20] G. Dajaku, and D. Gerling, "A novel tooth concentrated winding with low space harmonic contents," Proc. of IEEE International Electric Machines and Drives Conference (IEMDC), pp. 755-760, May 2013.
- [21] P. B. Reddy, H. Kum-Kang, and A. El-Refai, "Effect of stator shifting on harmonic cancellation and flux weakening performance of interior PM machines equipped with fractional-slot concentrated windings for hybrid traction applications," Proc. of IEEE Energy Conversion Congress and Exposition (ECCE), pp. 525-533, Sep. 2012.
- [22] J. Wang, "An Electric Machine," UK Patent, 1221635.4, Filed on Nov. 30, 2012.
- [23] X. Chen, J. Wang, P. Lazari, and L. Chen, "Permanent Magnet Assisted Synchronous Reluctance Machines with fractional-slot winding configurations," in Proc. of IEEE Electric Machines & Drives Conference (IEMDC), pp. 374-381, May 2013.
- [24] E. Levi, R. Bojoi, F. Profumo, H. A. Toliyat, and S. Williamson, "Multiphase induction motor drives – a technology status review," IET Electric Power Applications, Vol. 1, No. 4, pp. 489-516, Jul. 2007.
- [25] L. De Lillo, L. Empringham, P. W. Wheeler, S. Khawn-On, C. Gerada, M. N. Othman, and H. Xiaoyan, "Multiphase power converter drive for fault-tolerant machine development in aerospace applications," IEEE Trans. on Industrial Electronics, Vol. 57, No. 2, pp. 575-583, Feb. 2010.
- [26] M. G. Malti, and F. Herzog, "Fractional-slot and dead-coil windings," Trans. of the American Institute of Electrical Engineers, Vol. 59, No. 12, pp. 782-794, Dec. 1940.
- [27] J. Wang, Z. P. Xia, and D. Howe, "Analysis of three-phase surface-mounted magnet modular permanent magnet machines," 2nd International Conference on Power Electronics, Machines and Drives, Vol. 3, pp. 27-32, Mar.-Apr. 2004.
- [28] P. Morrison, A. Binder, B. Funieru, and C. Sabirin, "Drive train design for medium-sized zero emission electric vehicles," 13th European Conference on Power Electronics and Applications (EPE), pp. 1-10, Sep. 2009.
- [29] A. Vagati, G. Pellegrino, and P. Guglielmi, "Comparison between SPM and IPM motor drives for EV application," IEEE International Conference on Electrical Machines (ICEM), pp. 1-6, Sep. 2010.
- [30] V. I. Patel, J. Wang, W. Wang, and X. Chen, "Analysis and design of 6-phase fractional slot per pole per phase permanent magnet machines with low space harmonics," Proc. of IEEE International Electric Machines and Drives Conference (IEMDC), pp. 386-393, May 2013.
- [31] J. Wang, X. Yuan, and K. Atallah, "Design optimization of a surface mounted permanent magnet motor with concentrated windings for electric vehicle applications," IEEE Trans. on Vehicular Technology, Vol. 62, No. 3, pp. 1053-1064, Mar. 2013.
- [32] P. Lazari, J. Wang, and L. Chen, "A computationally efficient design technique for electric vehicle traction machines," IEEE International Conference on Electrical Machines (ICEM), pp. 2596-2602, Sep. 2012.



Vipulkumar I. Patel (S'13) was born in Kamana Village, Mahesana District, Gujarat, India in 1982. He received the B.E. in electrical engineering from Nirma Institute of Technology, Gujarat University, Ahmedabad, India in 2003 and M.Tech. in power electronics, electrical machines and drives from

Indian Institute of Technology, Delhi, India in 2005. He is currently pursuing the Ph.D. degree in electronic & electrical engineering at The University of Sheffield, Sheffield, U.K.

From 2005 to 2010, he was a Lead Engineer with GE India Technology Centre, Bangalore, India. His research interests include design and analysis of permanent-magnet machines for electric traction applications.

Mr. Vipulkumar was a recipient of the IEEE PEDES '96 Award for the best performance in the area of power electronics, electrical machines & drives in 2005.



Jiabin Wang (SM'03) received the B.Eng. and M.Eng. degrees from Jiangsu University of Science and Technology, Zhengjiang, China, in 1982 and 1986, respectively, and the Ph.D. degree from the University of East London, London, U.K., in 1996, all in electrical and electronic engineering. He is currently a

Professor of electrical engineering with The University of Sheffield, Sheffield, U.K.

From 1986 to 1991, he was with the Department of Electrical Engineering, Jiangsu University of Science and Technology, where he was appointed a Lecturer in 1987 and an Associated Professor in 1990. He was a Postdoctoral Research Associate with The University of Sheffield from 1996 to 1997 and a Senior Lecturer with the University of East London from 1998 to 2001. His research interests range from motion control to electromagnetic devices and their associated drives in applications ranging from automotive, household appliances, to aerospace sectors.



Weiya Wang received the B.Eng. degree in electrical and electronic engineering from Jiangsu University, Zhenjiang, China, in 1982, the M.Sc. degree in electronics and control systems from the University of East London, London, U.K., in 1996, and the Ph.D. degree in electrical and electronic engineering from The University of Sheffield, Sheffield, U.K., in 2006. She is currently a Research Associate with department of electronic and electrical engineering at The University of Sheffield, Sheffield, UK.

From 1982 to 1993, she worked for Jiangsu University, China, and appointed Lecturer in 1988. From 1997 to 2011, she was a Research Associate at The University of Sheffield, a Senior Research Fellow at Anglia Ruskin University, U.K. and a Senior Design Engineer at Mangnomatics Ltd., U.K. Her research interests include rotary, linear, and multiple degree-of-freedom motors and actuators and their control.



Xiao Chen (S'13) was born in Taian, Shandong Province, China, in 1988. He received the B.E. degree in electrical engineering from the Harbin Institute of Technology at Weihai, Weihai, China, in 2009 and the M.Sc. Degree in electrical engineering from the Harbin Institute of Technology, Harbin, China, in 2011 respectively. He is currently pursuing the Ph.D. degree in electronic & electrical engineering at The University of Sheffield, Sheffield, U.K. His research interest includes the permanent magnet machine design and modeling for the electric vehicle traction application.